Supporting Information

Nanostructural evolution of one-dimensional $BaTiO_3$ structures by hydrothermal conversion of vertically aligned TiO_2 nanotubes

J. A. Muñoz-Tabares,*[a] K. Bejtka,[a] A. Lamberti,[b] N. Garino,[a] S. Bianco,[b] M. Quaglio,[a] C. F. Pirri[ab] and A. Chiodoni*[a]

[a]Center for Space Human Robotics (CSHR), Istituto Italiano di Tecnologia, Torino 10129, Italy. E-mail: jose.munoz@iit.it, j.a.munoz.tabares@gmail.com, angelica.chiodoni@iit.it

[b]Applied Science and Technology (DISAT), Politecnico di Torino, Torino 10129, Italy

Table S1 Complementary structural parameters for Ti and $BaTiO_3$ obtained from Rietveld refinement of *Zero*, *Weak*, *Medium* and *Strong* XRD spectra.[a]

	Hydrothermal conversion treatment			
	Zero	*Weak*	*Medium*	*Strong*
[KOH] (M)	0.05	0.25	0.25	1
T (°C)	150	150	200	200
Time (h)	2	2	24	24
	Microstructure			
Symmetry	Ti (P63/mmc) a=b=2.9488(1) Å c=4.6820(2) Å α=β=90°, γ=120°	$BaTiO_3$ (P4mm) a=b=4.03094(1) Å c=4.0370(2) Å α=β=γ= 90°	$BaTiO_3$ (P4mm) a=b=4.0178(1) Å c=4.0274(2) Å α=β=γ= 90°	$BaTiO_3$ (P4mm) a=b=4.0145(1) Å c=4.0252(4) Å α=β=γ= 90°
Atomic positions	---	Ba (0, 0, 0) Ti (0.5, 0.5, 0.550(2)) O_I (0.5, 0.5, 0.0[b]) O_{II} (0.5, 0, 0.5[b])	Ba (0, 0, 0) Ti (0.5, 0.5, 0.555(2)) O_I (0.5, 0.5, 0.983(1)) O_{II} (0.5, 0, 0.489(2)	Ba (0, 0, 0) Ti (0.5, 0.5, 0.557(2)) O_I (0.5, 0.5, 0.977(2)) O_{II} (0.5, 0, 0.488(1))
Tetragonality	---	1.00150	1.00239	1.00266
Volume cell (Å^3)	---	65.59	65.01	64.87
Crystal Size (nm)	254(4)	54(1)	66(3)	92(6)
MicroStrain (%)	-0.116(3)	0.345(8)	0.209(6)	0.101(9)
	Composition (%)			
$BaTiO_3$	---	80.4(7)	81.5(3)	84.7(3)
Ti	45.04(7)	5.3(4)	5.6(6)	4.3(1)
$BaCO_3$	---	0.8(7)	1.34(6)	4.4(1)
$BaTi_4O_9$	---	---	0.66(6)	1.1(1)
Ba_2TiO_4	---	---	1.0(1)	2.9(1)
$BaTi_5O_{11}$	---	---	1.8(3)	2.6(4)
Amorphous TiO_2	54.96(7)	13.5(1)	8.1(2)	---

[a]The errors for refined parameters are given in brackets. [b]Unrefined parameters.

Table S2 Thickness of the TiO_2-NTs/Converted-NTs layer as measured by means of TEM.

TiO2-NTs/*Zero*	*Weak*	*Medium*	*Strong*
5.85±0.06	4.76±0.06	---	4.05±0.03

Fig. S1 Details of the *Strong* XRD spectrum between 23.2° and 31° (2θ), which corresponds to the range of maximum intensities of the minor phases, where (♦) $BaCO_3$, (♣) Ba_2TiO_4 , (♠) $BaTi_4O_9$ and (♥) $BaTi_5O_{11}$.

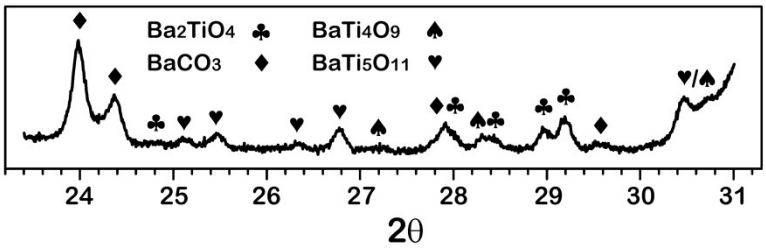

S.1. Evolution of the crystallographic structure during hydrothermal conversion of TiO_2-NTs

S.1.1. On the signal contribution due to adsorption and the effects on phase quantification

The important signal contribution from the Ti substrate (**Table S1**) was attributed to the high transparency of the amorphous TiO_2-NT layer. In this sense, the X-ray penetration depth to attain a maximum intensity of 99% (Beer–Lambert law) for TiO_2 amorphous can be estimated as 8 and 27 µm for 20° and 70° (2θ), respectively, if it is assumed a density (ρ) of 3.80 g/cm^3 and a mass attenuation coefficient (µ/ρ) of 129 cm^2/g for the aforementioned phase. Such a penetration depth is almost five times that of the TiO_2-NT layer thickness, which was estimated as 5.85(6) µm by means of TEM (**Table S2**), thus indicating that an important volume of substrate was illuminated during the XRD data acquisition. In contrast, the converted NT layer of the *Weak*, *Medium* and *Strong* samples presents a higher opacity, as this is mainly composed of $BaTiO_3$ (without an amorphous phase), and has a density (ρ) of 5.97 g/cm^3 and a mass attenuation coefficient (µ/ρ) of 239 cm^2/g. In this case, the X-ray penetration depth necessary to attain a maximum intensity of 99% was estimated as 3 and 9 µm for 20° and 70° (2θ), respectively. This penetration depth is only twice the thickness of the $BaTiO_3$-NTs layer (~4.5 µm) for the *Strong* sample (Table S2), which means less substrate volume is illuminated by the X-rays. Considering this, it is expected that the signal from a sample with a fully-transformed NT layer irradiated with X-rays show a lower contribution from the substrate (Ti concentration) than a partially transformed layer, because of its higher absorption capability. This trend has been observed for the *Weak* and *Medium* samples, which also exhibit the presence of an amorphous TiO_2 phase (13.5 and 8.1%, respectively).

S.1.2. The "size effect" of nanosized $BaTiO_3$

As far as the crystal structure is concerned, the "size effect" of nanosized $BaTiO_3$ is a phenomenon that has been well documented in literature. This phenomenon involves a decrease in ferroelectricity as the crystallite size decreases. This behaviour has been explained by means of a core/shell model, in which the particle surface is composed by a cubic phase shell separated from the tetragonal core for a gradient lattice strain layer (GLSL).[S1] The ferroelectricity disappears below a critical size, because the particles lose their cores as the cubic walls join together.[S1] This surface layer of cubic phase occurs as a mechanism to reduce the surface energy.[S2,S3] In this sense, it has been shown that the cubic-phase presents a lower surface energy, especially TiO_2-terminated surfaces, than the tetragonal phase.[S2,S3] Taking all this into consideration, a multiphase model with a mix of tetragonal (P4mm symmetry, space group 99) and cubic (Pm-3m symmetry, space group 221) phases was applied during the early refinement stages of the *Weak*, *Medium* and *Strong* XRD spectra in order to fit the $BaTiO_3$ reflections. This approach gave correct fittings, with an R_{wp} of about 9%. However, better results were obtained for a single phase model (tetragonal) with R_{bragg} and χ^2 equal to 1.61 and 2.24 % for the *Weak* sample, 1.32 and 4.19 % for the *Medium* sample and 1.61 and 6.23 % for the *Strong* sample, respectively. Therefore, a single phase model was eventually set up considering only the tetragonal phase.

S.2. Evolution of the morphology during hydrothermal conversion of TiO_2-NTs.

S.2.1. Characterization of the Ti-rich barium titanate phases

The FFT obtained from the Ti-rich area (green) in Figure 4 exhibits a hexagonal arrangement with poorly defined spots. By analysing the HRTEM filtered experimental image (**Figure S2**), it was possible to measure three main inter-planar distances equal to 0.286, 0.296 and 0.3303 nm. Of these, only the first one could be assigned to the {110} planes of $BaTiO_3$, while the other two (0.296 and 0.3303 nm) clearly did not belong to any $BaTiO_3$ family of planes. These distances were then correlated to the Ti-rich barium titanate phases, that is, $BaTi_5O_{11}$ and $BaTi_4O_9$. Adopting this approach, two possible orientations were selected to index the Ti-rich phase FFT.

The first orientation corresponds to the $BaTiO_5O_{11}$ phase along the [3-23] zone axis (highlighted in light green in Figure S2), while the second possible orientation, for $BaTi_4O_9$, was the [-231] axis zone (highlighted in yellow). In order to define a single indexation for the Ti-rich area, HRTEM images of both possible structures were simulated in the aforementioned zone axes and compared with the filtered experimental image (upper right corner in Figure S2). As can be seen from this comparison, both structures show a similar contrast as the experimental image. Unfortunately, this approach did not allow one of these two phases to be unambiguously assigned because of the high concentration of defects observed in this area, especially for 0.296 and 0.303 nm distances. Such a defects cause an irregular contrast in the experimental image, as is evidenced by the digital dark field decomposition of the HRTEM (**Figure S3**), which difficult the correct indexation.

S.2.2. Dissolution-precipitation as conversion mechanism of TiO_2 into $BaTiO_3$

Dissolution-precipitation as a mechanism of TiO_2 conversion into $BaTiO_3$, has been discussed extensively in the literature. In this mechanism, the TiO_2 precursor is dissolved, via hydrolytic attack of the Ti-O bonds, to form soluble hydroxytitanium complexes $Ti(OH)_x^{(4-x)+}$. These complexes enter solution and are capable of reacting with Ba^{2+} ions to precipitate into $BaTiO_3$ according to the following overall reaction:

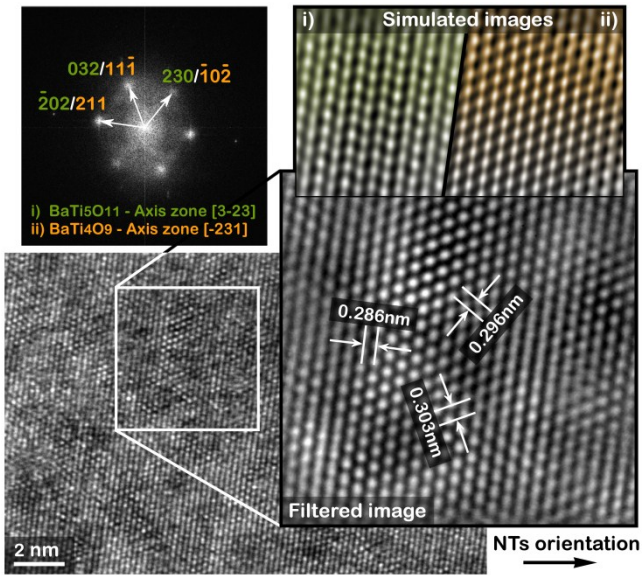

Fig. S2 HRTEM image obtained from the Ti-rich area (green) in Figure 4. FFT (at the top) exhibits a hexagonal arrangement with poorly defined spots. The corresponding inter-planar distances were obtained from the filtered experimental image (on the right). Simulated images of the two possible structures, indexed as $BaTi_4O_9$ along the [-231] axis zone (yellow) and $BaTi_5O_{11}$ along the [3-23] axis zone (light green), are shown in the upper right.

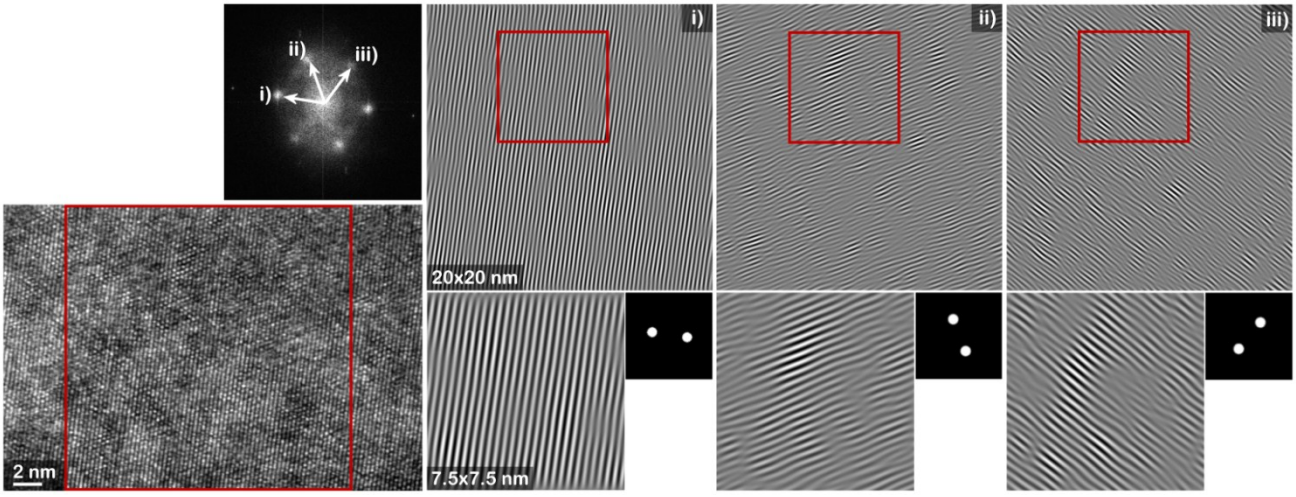

Fig. S3 On the left, HRTEM image of the Ti-rich phase (Figure 5 and the area highlighted in green in figure 4) and the corresponding FFT obtained from the area highlighted within the red frame, which shows poorly defined spots. i), ii) and iii) correspond to the digital dark field decomposition obtained by means of selective masking and filtering of the FFT (where only a couple of spots were selected each time). From these images, it is possible to observe an important concentration of dislocation for planes ii) and iii), which correspond to inter-planar distances of 0.296 and 0.303 nm, respectively. The family of planes closest to $BaTiO_3$ (with an inter-planar distance of 0.286 nm and labelled as i) presents a significantly lower concentration of defects.

$$Ba^{2+} + Ti^{4+} + 6OH^- \rightleftharpoons BaTiO_3 + 3H_2O \quad \text{(S1)}$$

This reaction step involves the following reactions and equilibria, as was determined from the phase stability diagrams (pH, temperature and concentration) obtained from the thermodynamic study by Lencka and Riman.[S4]

$$H_2O \rightleftharpoons H^+ + OH^- \quad \text{(S2)}$$

$$Ba(CH_3OO)_2 \rightleftharpoons Ba^{2+} + 2CH_3COO^- \quad \text{(S3)}$$

$$TiO_2(s) + 2H_2O \rightleftharpoons Ti(OH)_x^{(4-x)+} + (4-x)OH^- \quad \text{(S4)}$$

$$Ti(OH)_x^{(4-x)+} \rightleftharpoons Ti^{4+} + (4-x)OH^- \quad \text{(S5)}$$

$$KOH \rightleftharpoons K^+ + OH^- \quad \text{(S6)}$$

Several studies on the reaction kinetics of this system have shown that the *dissolution-precipitation* mechanism is rate-limited by boundary phase reactions between the reagents in static conditions or by the formation of nucleation sites in non-static conditions.[S5] These two limiting regimens are characterized by slopes *m* of ≈1 and >1, respectively, in the Johnson-Mehl-Avrami plots, as proposed by Hancock and Sharp.[S6] In the case of reactions without stirring (static), as in the present case, the rate limiting process has been related to the dissolution/hydrolysis of TiO_2,[S5] which occurs at the liquid/solid interface. As far as this aspect is concerned, it has been shown that

amorphous TiO_2 dissolves faster than crystalline TiO_2 (both rutile and anatase),[S7] due to the higher bond energy and less exposed area of the crystal compared to the amorphous phase. Additionally, some of the above works reported a second stage of crystallization, which is characterized by a slope *m* <0.5. Such a regimen has not been assigned to any of the three distinct reaction mechanisms proposed by Hancock and Sharp[S6] and has been attributed to the competition of multiple mechanisms (*in situ* and *heterogeneous* precipitation).[S8]

S.2.3. Diffusion of Ba atoms during hydrothermal conversion of TiO_2 nanotubes

Figure S4 presents the atomic percentage profiles for Ba, Ti and Ga species obtained by means of EDX in STEM mode on *Weak* and *Strong* samples. Owing to the porosity of the sample (which reduces the effective volume), spectrum acquisition by area was chosen over a continuous profile, which gives a better signal/noise ratio. Each experimental point on the profile thereby corresponds to a spectrum obtained from an area of approximately 600x600 nm. The acquisition was performed consecutively, starting, as the first acquisition step, from the area closest to the surface and going down to the bottom, as indicated by dotted frames on the STEM images at the bottom of Figure S4.

Both samples in these plots present an increment in the Ti content from the top to the bottom, which could be related to the higher density at the bottom due to the decrease in the inner diameter from the top (107±3 nm) to the bottom (36±3 nm), as described in the main text, and/or a higher thickness of the sample due to the sample preparation procedure. As far as the Ba profile is concerned, a higher Ba content was found in the *Weak* sample in the first micron from the surface. This area corresponds to the blurred structure in which rounded $BaTiO_3$ grains of about 50 nm in size were found (see Figure 3 in the main text). The Ba content in the subsequent microns presents a sharp drop, up to ~20% of the initial value, and remains approximately constant along the rest of the length of the sample, which still exhibits the initial tubular structure. This is a clear indication of the fact that the reaction between the TiO_2 nanotubes and the Ba solution had mainly occurred in the first microns. The fact that some Ba was also detected at the bottom of the sample could be correlated to the presence of Ba solution drops, which have entered the tubes (Figure S4, see the long white contrast grains on the *Weak* sample). On the other hand, the *Strong* sample also presented a higher Ba content in the areas closest to the surface. However, in this case, a slight decay was observed without sharp drops. This more homogeneous profile of Ba is therefore a clear indication of the precursor solution having infiltrated along the whole length of the sample and of having completed the hydrothermal conversion of the nanostructure.

Regarding the presence of Ga implanted ions, it is clear, from the EDX profiles, that the Ga signal was present in both samples, even though the content was quite low and constant along the length of the nanostructures. This result demonstrated that the procedure applied to prepare the samples guarantees a minimal incidence of implanted Ga ions and, hence, the presence of an amorphous surface layer.

S.2.4. On the Ba_2TiO_4 formation

So far, the described mechanism has cast new light on the formation of all the identified phases (main and minor), except Ba_2TiO_4. This phase has been observed during the synthesis of $BaTiO_3$ by means of solid-state reactions of mixed $BaCO_3$ and TiO_2 powders at high temperatures,[S9] where Ba_2TiO_4 is a secondary phase that is formed during the reaction due to compositional in-homogeneities at a local level.[S9] In the case of hydrothermal synthesis, the phase diagrams (pH vs composition) determined by Lencka et. al.[S4] show that, in the presence of CO_2, the stable phase is $BaCO_3$ over $BaTiO_3$. Thus, in the case of a closed system with a limited CO_2 content (as in the present case), both phases coexist stably,[S4] once $BaCO_3$ has precipitated and the CO_2 source is exhausted. In addition, previous works have shown

Fig. S4. Atomic percentage profiles for Ba, Ti and Ga species on: A) *Weak* and B) *Strong* samples, obtained by means of EDX. Each experimental point corresponds to a spectrum obtained from an area of approximately 600x600 nm, which is indicated by dotted frames on the STEM images at the bottom.

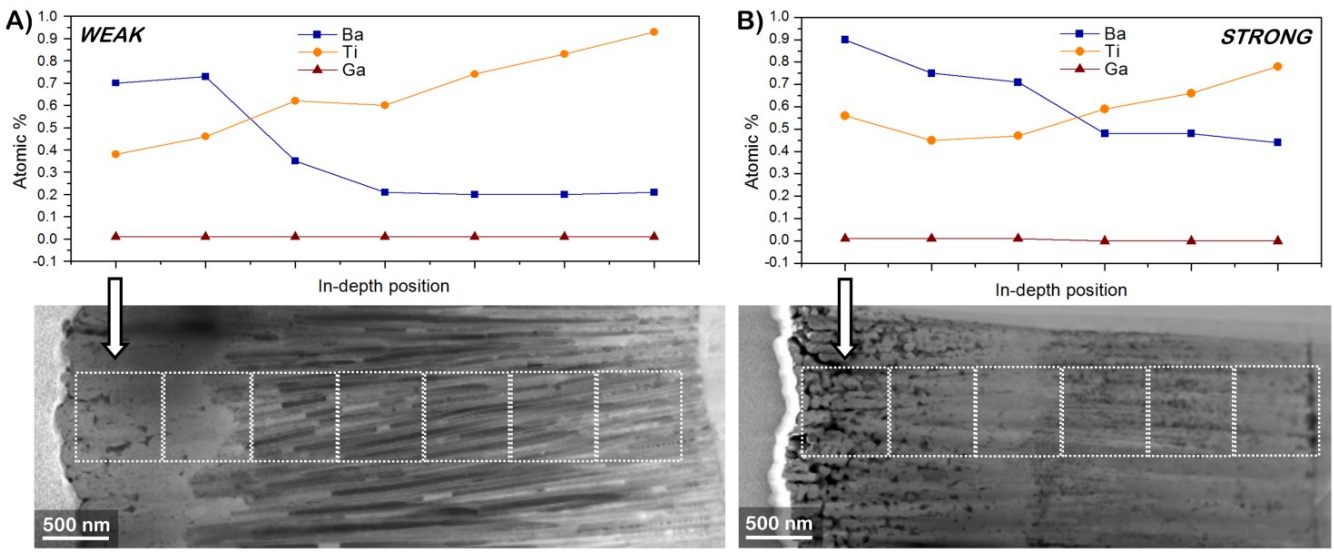

that there is no relationship between the type of barium titanate precipitated by means of hydrothermal synthesis and the Ba/Ti ratio of the initial reagents,[S8,S10] thus pure $BaTiO_3$ was obtained for Ba/Ti ratios >1 .[S10] Bearing this in mind, it is possible to suggest that the observed Ba_2TiO_4 phase is an intermediate product, which is produced during the formation of $BaCO_3$ from the reaction of already formed $BaTiO_3$ (solid) and CO_2 previously absorbed into the NT structure, by means of reactions (S7) and (S8), and is not a product of the local compositional in-homogeneities (i.e. a local excess of Ba).

$$2BaTiO_3 \xrightarrow{CO_2} Ba_2TiO_4 + TiO_2 \quad \text{(S7)}$$

$$Ba_2TiO_4 + CO_2 \not\rightarrow BaCO_3 + BaTiO_3 \quad \text{(S8)}$$

Notes and references

S1 T. Hoshina, S. Wada, Y. Kuroiwa, and T. Tsurumi, *Appl. Phys. Lett.* 2008, **93**, 192914.
S2 J. Padilla and D. Vanderbilt, *Phys. Rev. B.* 1997, **56**, 1625.
S3 R. I. Eglitis, G. Borstel, E.·Heifets, S. Piskunov and E. J. Kotomin, *Electroceram.* 2006, **16**, 289.
S4 M. M. Lencka and R. E. Riman, *Chem. Mater.* 1993, **5**, 61.
S5 F. Maxim, P. M. Vilarinho, P. Ferreira, I. M. Reaney and I. Levin, *Cryst. Growth Des.* 2011, **11**, 3358.
S6 J. D. Hancock and J. H. Sharp, *J. Am. Ceram. Soc.* 1972, **55**, 74.
S7 I. J. Clark, T. Takeuchi, N. J. Ohtoric and D. C. Sinclair, *Mater. Chem.* 1999, **9**, 83.
S8 J. O. Eckert Jr., C. C. Hung-Houston, B. L. Gersten, M. M. Lencka and R. E. Riman, *J. Am. Ceram. Soc.* 1996, **79**, 2929.
S9 A. Beauger, J. C. Mutin and J. C. Niepce, *J. Mater. Sci.* 1983, **18**, 3041.
S10 N. A. Ovramenko, L. I. Shvets, F. D. Ovcharenko and B. Y. Kornilovich, *Neorg. Mater.* 1979, **15**, 1982.

Fig. S5. HRTEM image of a Ba_2TiO_4 crystal along the [010] axis zone found at the bottom of the TiO_2-NTs array after the *Strong* treatment.

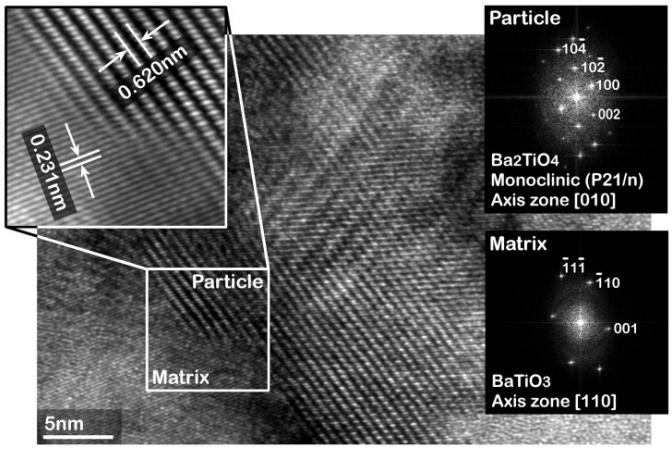

Fig. S6. HRTEM of the area between two sub-grains in a dendritic structure at the top of the *Strong* sample. A clear grain boundary can be observed between these particles, although they present a coherent crystallographic orientation, where both grains are oriented along the [112] axis zone.